Direct discrimination of structured light by humans

Dusan Sarenac[a,1], Connor Kapahi[a,b], Andrew E. Silva[c], David G. Cory[a,d], Ivar Taminiau[a], Benjamin Thompson[c], and Dmitry A. Pushin[a,b]

[a]Institute for Quantum Computing, University of Waterloo, Waterloo, ON N2L3G1, Canada; [b]Department of Physics and Astronomy, University of Waterloo, Waterloo, ON N2L3G1, Canada; [c]School of Optometry and Vision Science, University of Waterloo, Waterloo, ON N2L3G1, Canada; and [d]Department of Chemistry, University of Waterloo, Waterloo, ON N2L3G1, Canada

Edited by Michael Berry, University of Bristol, Bristol, United Kingdom, and approved May 20, 2020 (received for review November 17, 2019)

We predict and experimentally verify an entoptic phenomenon through which humans are able to perceive and discriminate optical spin–orbit states. Direct perception and discrimination of these particular states of light with polarization-coupled spatial modes is possible through the observation of distinct profiles induced by the interaction between polarization topologies and the radially symmetric dichroic elements that are centered on the foveola in the macula of the human eye. A psychophysical study was conducted where optical states with a superposition of right and left circular polarization coupled to two different orbital angular momentum (OAM) values (ℓ_1 and ℓ_2) were directed onto the retina of participants. The number of azimuthal fringes that a human sees when viewing the spin–orbit states is shown to be equal to the number (N) of radial lines in the corresponding polarization profile of the beam, where $N = |(\ell_1 - \ell_2) - 2|$. The participants were able to correctly discriminate between two states carrying OAM $=7$ and differentiated by $N = 5$ and $N = 9$, with an average success probability of 77.6% (average sensitivity $d' = 1.7$, $t(9) = 5.9$, $p = 2 \times 10^{-4}$). These results enable methods of robustly characterizing the structure of the macula, probing retina signaling pathways, and conducting experiments with human detectors and optical states with nonseparable modes.

human perception | orbital angular momentum | spin–orbit coupling

Custom light fields, also known as "structured light," can be engineered to achieve nontrivial propagation properties such as orbital angular momentum (OAM), nondiffraction, self-healing, and self-imaging (1–5). In particular, the emergence of helical waves carrying OAM (6, 7) has enabled numerous applications in microscopy, high-bandwidth communication, material characterization, and manipulation of matter (8–13). It is also possible to create structured light that is coupled in polarization and OAM (14–16). These so-called "spin–orbit states" or "vector vortex beams" possess space-varying polarization profiles, and they have found applications in high-resolution imaging and optical metrology (17–19).

Here we consider the physiology of human vision and optical spin–orbit states. The techniques explored in this work bring the vast toolbox of structured light to visual science applications. We experimentally verify an entoptic phenomenon through which humans can perceive and discriminate between different spin–orbit states when directly viewing them. Direct discrimination is possible through the perception of distinct entoptic images that are induced by space-varying polarization. The behavior and form of the two-dimensional polarization topologies that arise when there is a superposition of polarization states coupled to different OAM values has been thoroughly studied in the literature (20–23). A pictorial representation of our experiment is shown in Fig. 1*A*, where optical states composed of a coherent superposition of differently polarized planar and helical waves carrying OAM were directed onto the retina of the observers. These spin–orbit states are nonseparable in polarization and spatial modes (24, 25). When considering light (as in the case of our experiment), this terminology refers to the way in which the scalar and vector aspects of light are combined in the optical beams: nonseparable in a product basis of scalar (particularly azimuthal phase) and vector (polarization) states. Note that the same terminology is used in quantum optics, to describe the same optical states, but in the context of experiments involving correlations between individual photons.

The ability to perceive space-varying polarization may be derived from an entoptic phenomenon through which humans can perceive the polarization state of light (26–29). When viewing polarized light, a bowtie-like shape (known as "Haidinger's brush") appears in the central point of the visual field. Although the exact physiological origin of the Haidinger's brushes is not fully understood, the prominent theory suggests that the perception of Haidinger's brushes depends on the presence of radially symmetric dichroic elements that are centered on the foveola (30). This has led to studies where Haidinger's brushes are used to assess central visual field dysfunction and age-related macular degeneration (31, 32), measure macular pigment density (33), and determine the location of the fovea (34).

The orientation of the Haidinger's brush depends on the polarization state of light. Linearly polarized light induces a brush oriented perpendicular to the polarization direction (26), while the brush appears rotated $\sim 45^\circ$ clockwise (counterclockwise) when viewing left (right) circularly polarized light (35). However, retinal adaptation causes Haidinger's brushes to disappear after a few seconds if the polarization direction relative to the eye does not change. It has been found that stable perception of the brushes is achieved when the linear polarization source is rotated at ~ 1 Hz (36). One may observe the behavior of Haidinger's brushes by looking at the light scattered in the

Significance

Recent technological advances have enabled the creation of custom light fields with remarkable properties. Here we report an experiment that merges human visual perception with structured wavefronts and optical states that are nonseparable in polarization and spatial modes of light. We demonstrate that humans are able to discriminate between two polarization-coupled orbital angular momentum states with a high probability when directly viewing a structured light beam. The work brings the techniques of structured light to visual science applications and paves the way for methods of characterizing the structure of the macula and conducting experiments with human detectors and optical states with nonseparable modes.

Author contributions: D.S. initiated the research; D.S., C.K., A.E.S., D.G.C., B.T., and D.A.P. designed research; D.S., C.K., A.E.S., and D.A.P. performed research; I.T. developed the spiral phase plate; D.S., C.K., A.E.S., D.G.C., B.T., and D.A.P. analyzed data; and D.S., C.K., A.E.S., D.G.C., I.T., B.T., and D.A.P. wrote the paper.

The authors declare no competing interest.

This article is a PNAS Direct Submission.

[1]To whom correspondence may be addressed. Email: dsarenac@uwaterloo.ca.

First published June 16, 2020.

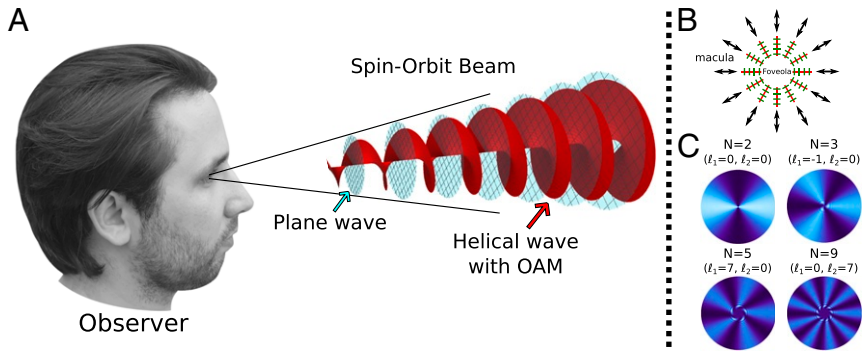

Fig. 1. (*A*) Pictorial representation of a spin–orbit beam, composed of a coherent superposition of a planar right-circularly polarized state and a helical left-circularly polarized state, being directed onto the retina of an observer. The helical state carries OAM, and its phase varies along the azimuthal coordinate ϕ. The depicted example corresponds to Eq. **1** with $\ell_1 = 0$ and $\ell_2 = -1$. (*B*) In the macula of the human eye, the macular pigment molecules (green) are bound to the radially oriented Henle fibers (red) that surround the foveola. The radial symmetry of these dichroic elements (polarization filter direction as a function of the azimuthal coordinate is shown by black arrows) coincides with the symmetry of the polarization-coupled OAM beams shown in *A*. (*C*) The number of azimuthal fringes that a human sees when viewing the spin–orbit beams is equal to the number of radial lines (*N*) in the corresponding polarization profile of the beam, where $N = |(\ell_1 - \ell_2) - 2|$. Shown are the examples for $N = 2$ where $\ell_1 = \ell_2 = 0$, $N = 3$ where $\ell_1 = -1$, $\ell_2 = 0$, $N = 5$ where $\ell_1 = 7$, $\ell_2 = 0$, and $N = 9$ where $\ell_1 = 0$, $\ell_2 = 7$. The size of the central region increases with propagation. The $N = 2$ case depicts the Haidinger's brush profile when horizontally polarized light is observed.

clear sky $\sim 90^\circ$ from the sun (37). With some practice, a brush may be observed that points toward the sun.

Here we consider spin–orbit states that are composed of a coherent superposition of differently polarized planar and helical waves. The wavefunction of a spin–orbit state traveling along the z direction can be written as

$$|\Psi\rangle = \frac{1}{\sqrt{2}}\left[C_1(\ell_1, r, z)e^{i\ell_1\phi}|R\rangle + C_2(\ell_2, r, z)e^{i\ell_2\phi}|L\rangle\right], \quad [1]$$

where we have used the bra–ket notation for convenience, $|L\rangle = \begin{pmatrix}0\\1\end{pmatrix}$ and $|R\rangle = \begin{pmatrix}1\\0\end{pmatrix}$ denote the left and right circular polarization, and (r, ϕ) are the cylindrical coordinates. The form of the radial and propagation contributions, $C_1(\ell_1, r, z)$ and $C_2(\ell_2, r, z)$, depends on the method used to prepare the OAM beams. Exact forms have been shown for the Laguerre Gauss modes (6) and beams reflected from a spiral phase plate (SPP) (38).

As shown in Fig. 1*B*, the macular pigment molecules (green) in the human macula are bound to the radially oriented Henle fibers (red) that surround the foveola (30). The accepted model for the action of the macula on the incoming light is to treat it as a radial polarization filter (39–41), a concept dating back to Maxwell and Helmholtz (42, 43). The operator of the macula can therefore be expressed as

$$|M\rangle\langle M| = \frac{1}{2}\begin{pmatrix}1 & e^{-i2\phi}\\ e^{i2\phi} & 1\end{pmatrix}. \quad [2]$$

Several theories have been put forward in order to account for the human perception of circularly polarized light. Good agreement is found when accounting for corneal birefringence that is uniformly along the visual axis (39, 44, 45). The corresponding operator is given by

$$U_m = e^{i\frac{\alpha}{2}\hat{\sigma}_x}, \quad [3]$$

where $\hat{\sigma}_x$ is the Pauli operator. The clarity of the brush when viewing circularly polarized light is determined by the total amount of phase (α) that the ocular birefringence induces, which is subject to individual variation (39, 44, 45). The two operators of Eqs. **2** and **3** acting on a polarized light beam reproduce, with good agreement, the reported descriptions of the Haidinger's brushes and polarization gradients (26–29).

It follows that the profile that a person would perceive when viewing a spin–orbit beam is given by

$$I = |\langle M|U_m|\Psi\rangle|^2, \quad [4]$$

where $|\Psi\rangle$ is given by Eq. **1**. The radial symmetry of the macula in the human eye coincides with the symmetry of polarization-coupled OAM states. The eye operator in Eq. **2** possesses an $e^{i2\phi}$ term, whereas OAM states are associated with a helical phase front which is described by the factor $e^{i\ell\phi}$ in the wave function, where ϕ is the azimuthal coordinate and ℓ is the OAM value.

The schematic of the experimental setup is shown in Fig. 2. The laser light was attenuated to < 1 $\mu W/mm^2$ at the location of the observer in order to conform to the guidelines for laser exposure time outlined by the International Commission on Non-Ionizing Radiation (46). An SPP (47) was placed in one arm of a Michelson interferometer along with standard polarization components. The SPP in reflection mode induced OAM of $\ell = 7$ for $\lambda = 450$-nm light. The setup thus allowed us to prepare and switch between the following two spin–orbit states:

$$|\Psi_+\rangle = \frac{1}{\sqrt{2}}\left[C_1(7, r, z)e^{i7\phi}|R\rangle + C_2(0, r, z)e^{i\theta(t)}|L\rangle\right],$$
$$|\Psi_-\rangle = \frac{1}{\sqrt{2}}\left[C_2(0, r, z)e^{i\theta(t)}|R\rangle + C_1(7, r, z)e^{i7\phi}|L\rangle\right], \quad [5]$$

where $\theta(t)$ is a phase that varies linearly in time and acts to rotate the polarization profile of the beam, analogous to rotating the polarization direction of a beam to induce high-clarity Haidinger's brush (36). By translating the mirror along the beam propagation direction, we varied $\theta(t)$ with a speed of $\sim 2\pi$ rad/s. For a complete description of the parameters in the setup, see *Setup and Stimuli*. For the two states of Eq. **5**, we can determine the profiles that a person would observe using Eq. **4**. The two simulated profiles are shown in Fig. 1*C* under the labels "$N = 5$" for $|\Psi_+\rangle$ and "$N = 9$" for $|\Psi_-\rangle$. Therefore, a person may discriminate between the two states of Eq. **5** by observing the number of azimuthal fringes: $|\Psi_+\rangle$ state manifests five azimuthal fringes,

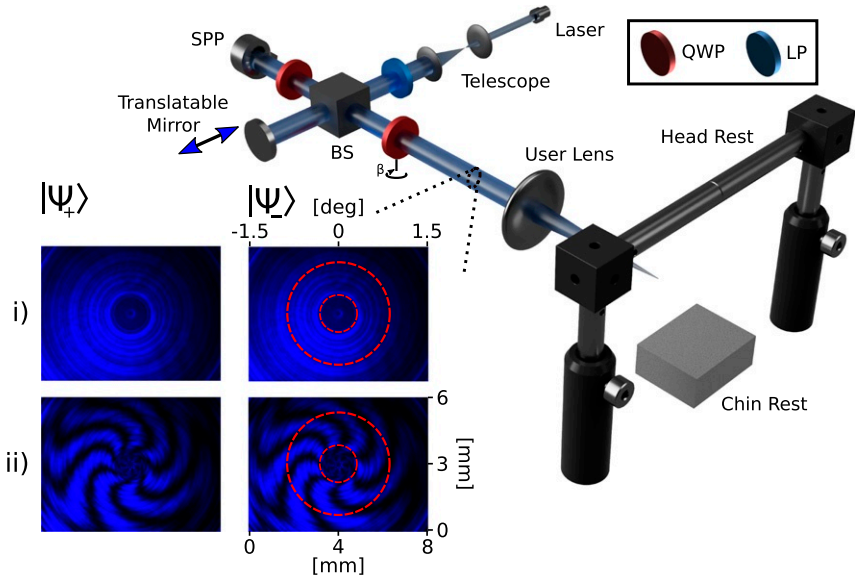

Fig. 2. Schematic of the experimental setup where a Michelson interferometer along with an SPP and standard polarization optics components are used to prepare the spin–orbit states that are directed onto the retina of the participants in the study. For a complete description of the setup, see *Setup and Stimuli*. Translating the mirror along the beam path direction varies $\theta(t)$ in Eq. **5**, while the two orientations of the outer QWP, $\beta \in [0, 180^\circ]$ around the vertical axis, correspond to the two states ($|\Psi_+\rangle$ and $|\Psi_-\rangle$) of Eq. **5**. (*i*) The images observed by a complementary metal–oxide semiconductor (CMOS) camera placed before the user lens, for both $|\Psi_+\rangle$ and $|\Psi_-\rangle$. It can be noted that azimuthal fringes are not present. The ring features are artifacts from SPP machining, and they are equally present in both images. (*ii*) The images observed by a CMOS camera placed before the user lens when a linear polarizer (LP) is placed in front of the camera. The seven azimuthal fringes correspond to the helical (OAM = 7) phase structure of $|\Psi_+\rangle$ and $|\Psi_-\rangle$, the only notable difference being the 180° azimuthal phase shift. The attenuators were removed to obtain the images shown in *i* and *ii*, and the camera gain was correspondingly optimized. In the study, the participants only observed beams shown in *i*, and the red circles bound the area (~2° of field of vision) with good intensity and high-quality phase structure that the participants were instructed to observe. The two simulated profiles of what the participants were expected to observe are shown in Fig. 1*C* under the labels "$N = 5$" for $|\Psi_+\rangle$ and "$N = 9$" for $|\Psi_-\rangle$. Note that the characteristic spherical phase of a Michelson interferometer caused the azimuthal fringes to wind.

and $|\Psi_-\rangle$ state manifests nine azimuthal fringes. Furthermore, it can be noted that the number of azimuthal fringes that a human sees when viewing the spin–orbit beams is equal to the number of radial lines (N) in the corresponding polarization profile of the beam, where $N = |(\ell_1 - \ell_2) - 2|$ (20–23). The observable is proportional to the difference in the OAM values which manifests itself as a number of entoptic azimuthal fringes. In order to determine the OAM value of the helical beam, an observer would be required to know the polarization state of the reference beam, as both ($\ell_1 = 0$, $\ell_2 = 7$) and ($\ell_1 = -7$, $\ell_2 = 0$) induce nine azimuthal fringes: $N = |(0 - 7) - 2| = 9$ and $N = |(-7 - 0) - 2| = 9$. Or, if the setup enabled the perception of the azimuthal fringes in the first diffraction ring, then, as shown in Fig. 1*C*, the OAM value can be determined by observing the number of azimuthal fringes along with their winding direction in the first ring.

To test the hypothesis that human observers can discriminate between the two states of Eq. **5**, a psychophysical study was conducted where randomly selected states (either $|\Psi_+\rangle$ or $|\Psi_-\rangle$) were presented, and participants discriminated between the two states based on the number of azimuthal fringes that they observed. Several factors helped ensure that the number of azimuthal fringes was the only cue for discriminating the beams. The setup used the orientation of the outer quarter wave plate (QWP) to change between $|\Psi_+\rangle$ and $|\Psi_-\rangle$ while keeping the same SPP configuration. This ensured that the ring features noticeable in Fig. 2, *i* were equally present in both cases. The studies were done without any ambient light, and there was a screen (with a 1-inch-diameter hole for the laser light to travel through) before the user lens which blocked the view of the setup by the participant. Furthermore, the QWP whose orientation determined which state was being observed was motorized to make an equal amount of motion between each trial. For a complete description of the psychophysical procedure, see *Psychophysical Procedure*.

After a brief familiarization period, the participants performed 100 random trials with structured light over two sessions on separate days. After viewing the stimulus, participants responded in one of two ways, responding "many" if they observed nine rotating azimuthal fringes, or responding "fewer" if they observed five rotating azimuthal fringes. Fig. 3 shows the results for the 10 participants who completed the study. There

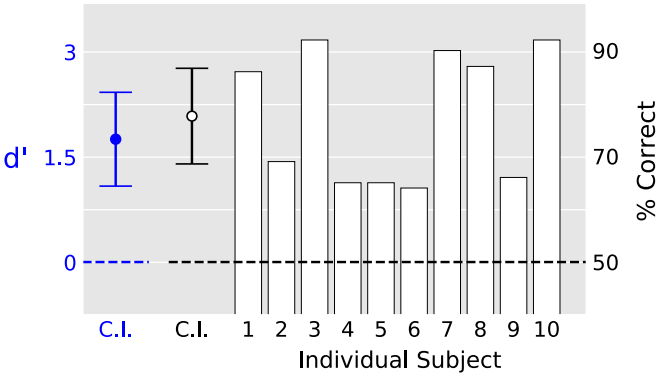

Fig. 3. Sensitivity and accuracy for the discrimination task. Each participant performed 100 trials over two sessions. The dashed line indicates chance performance. Open bars show individual participant performance. Circular symbols show group mean sensitivity (blue: left ordinate) and accuracy (black: right ordinate). Error bars show 95% CIs. Participants were highly sensitive to the difference between both trial types, performing significantly better than chance.

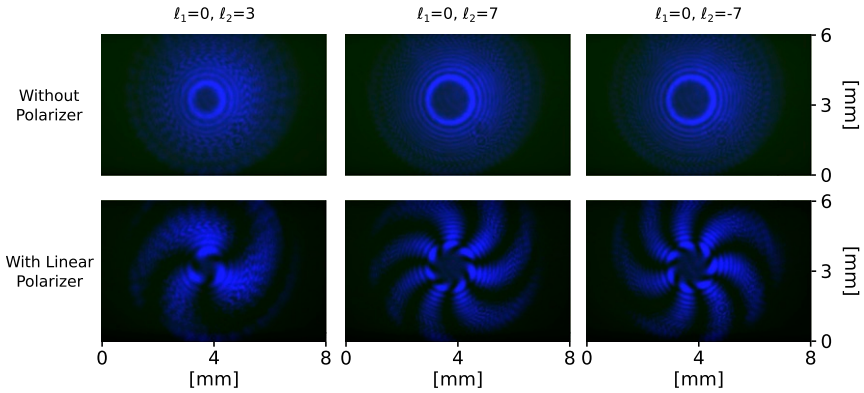

Fig. 4. Comparison of spin–orbit states generated with the setup of Fig. 2 using a SLM in place of the SPP. The topological charge of the fork dislocation pattern on the SLM sets the OAM value of the diffraction orders. Imaged is the intensity between the first diffraction order and the reference beam (*Top*) without a linear polarizer before the camera and (*Bottom*) with a linear polarizer before the camera. Shown are the examples for $\ell_1 = 0$, $\ell_2 = 3$, $\ell_1 = 0$, $\ell_2 = 7$, and $\ell_1 = 0$, $\ell_2 = -7$. Note that only the stimuli shown in Fig. 2 were presented to the observers during the study.

was no statistical difference between the results of session 1 and session 2, and therefore the data from both sessions were collapsed for the main analysis.

Sensitivity d' and response bias c were calculated for each participant. Percent correct is influenced by both a participant's ability to perform the task and the participant's response bias. However, d' is independent of response bias and is therefore a more accurate measure of performance when response bias is present (48). Data were analyzed using two-tailed, one-sample t tests with nine degrees of freedom (DOF) against the null value of 0.

All participants achieved performance that is numerically above chance, and, collectively, they achieved good discrimination sensitivity, $d' = 1.7$, $t(9) = 5.9$, P value $p = 2 \times 10^{-4}$, corresponding to a mean accuracy of 77.6 % correct. A significant response bias was also observed, $c = -0.2$, $t(9) = 3.0$, $p = .02$, as participants responded "many" more often than "fewer." Fig. 3 also suggests a bimodal distribution, where half of the participants achieved near-ceiling performance and the other half exhibited lower scores but remained above chance. There are no apparent explanations for this subdivision in terms of gender, age, or vision. We speculate that task performance is related to the various degrees of sensitivity that result from individual differences in the amount of ocular birefringence and the organizational structure of the macula.

These experiments explore and provide confirmation of humans directly perceiving and discriminating optical spin–orbit states and structured light with nonseparable modes. Many follow-up experiments are enabled, given the recent advances in the control and manipulation of structured light. The setup in Fig. 2 can be advanced by incorporating a spatial light modulator (SLM) in place of the SPP. This would allow us to prepare arbitrary polarization gradients and test the psychophysical thresholds of human perception of polarization: the sensitivity distribution for a range of OAM values, individual differences in discrimination ability, and human sensitivity to other forms of structured light and polarization gradient patterns. Furthermore, optimizing the subjective clarity of the observed image allows us to determine the exact forms of Eqs. **2** and **3** for a particular person. The exact form of the operators is currently subject to debate (30, 39–41).

Our follow-up studies will also explore clinical applications of structured light perception. We speculate that structured light can be a highly sensitive probe of central visual field dysfunctions and age-related macular degeneration. The techniques could provide a basis for the rapid, objective, and accurate assessment of macular pigment structure. Current clinical assessment techniques such as Optical Coherence Tomography and the subjective report of visual field distortions are only sensitive to the presence of ocular disease after irreversible retinal damage has occurred (49). Macular pigment assessment may be clinically useful in disease screening settings because macular pigment changes have been associated with a number of retinal diseases, including macular degeneration. Similar to fundus imaging with polarized light (34, 50), we can devise objective photographic tests with structured light.

Lastly, we can contribute to the research that integrates human detectors with recent technological advances (51–54). Given the nonseparability of Eq. **5**, an experiment can be conducted where the correlations between the two DOF, polarization and OAM, are confirmed with the human eye as the detector. The rotation of the profile that would be observed in the following two cases should be identical: phase shift on the OAM DOF (induced by rotating the SPP) and the phase shift on the polarization DOF (induced by a properly aligned birefringent material).*

Materials and Methods

Setup and Stimuli. In order to perform a valid human experiment, we are required to use a setup where the two beams that are presented to the observers do not have any differing intensity variations. Otherwise, an observer has the possibility to distinguish different spin–orbit beams by noticing a number of other features such as radially dependent intensity profiles as well as the intensity variations throughout the beam due to diffraction and/or OAM dynamics.

Consider the spin–orbit states shown in Fig. 4 that are generated with our setup using an SLM in place of the SPP. The topological charge of the fork dislocation pattern on the SLM sets the OAM value of the diffraction orders. Imaged is the intensity between the first diffraction order and the reference beam. Several important things can be noted: 1) The spin–orbit beams manifest radial intensity variations as they propagate. 2) Helical beams carrying different OAM values manifest unique dark regions in the center, and recognizable radial intensity variations. 3) The negative and positive OAM values also have differing features as the azimuthal fringes wind in opposite directions. Furthermore, artifacts and imperfections in the setup manifest differently for the two cases. Therefore, in order to ensure a valid experiment, we use two beams with the same OAM values but coupled to opposite polarization states. In this scenario, the intensity variations and the diffraction-related effects are identical for both presented beams and could not be used as a cue.

The schematic of the setup is shown in Fig. 2. For this experiment, we adhere to the guidelines for laser exposure time outlined by the International Commission on Non-Ionizing Radiation Protection which state that

*Note that the use of single photons instead of laser light would require an extremely bright single photon source, as the intensity of the light at the location of the user lens was ∼2 nW.

the maximum permissible exposure for a human eye for blue wavelengths is 1 μW/mm^2 (46). Attenuators of neutral density = 3.5 were placed after the laser in the setup, and the intensity of light was $\sim$2.9 nW before the user lens. It was confirmed that the power density of light near the focal spot (near the eye location) was well below the stated limit. The apparatus was approved for use with human participants by the University of Waterloo Ethical Review Board following an assessment by the University of Waterloo Safety Office.

As the clarity of the Haidinger's brushes peaks for blue light of $\sim$460-nm wavelength, we used a diode laser with a central wavelength of 450 nm. A single-mode optical fiber was used to clean the beam which was then expanded to 1.25-cm diameter via a two-lens telescope system ($f_1 = 25$ mm, and $f_2 = 150$ mm). The beam was then passed through a vertical polarizer. A Michelson interferometer was used to prepare the states of Eq. **5**. The first beam splitter creates a coherent superposition of two paths. One of the paths is reflected by a mirror, and the other path is reflected by an SPP. The SPP was generated out of 4N purity aluminum in an ultraprecision machining center using custom diamond tooling. Temperature control was kept within 1 °C, and form accuracy was limited by the thermal expansion of the aluminum due to any thermal drift. The SPP used in the experiment was originally designed for experiments with $\lambda = 532$ nm. The actual step height of the SPP is 1,596 nm, and, over a 25-mm aperture, the form accuracy is $\pm$0.5 μm, and the finish is $\pm$15 nm.

A QWP was placed in front of the SPP in order to induce a polarization flip. Finally, a QWP was placed at the output of the Michelson interferometer in order to prepare the two states of Eq. **5**. The orientation of the QWP determined which output state was being prepared. The two orientations, $\beta \in [0, 180^\circ]$, correspond to the two states ($|\Psi_+\rangle$ and $|\Psi_-\rangle$) of Eq. **5**. Note that the QWP is oriented along 45° and 135° in the two cases, since β is the angle around the vertical axis. Hence, this QWP was placed on a rotation stage. A lens with $f = 150$ mm was used to direct the beam onto the retina of the participants. Several lenses ($f = 75, 100, 150, 200, 250, 400, 500$ mm) were tested by authors D. S. and C. K., who determined, based on their subjective perceptions of the structured light, that $f = 150$ mm was the optimal choice.

The mirror was placed on a translation stage in order to induce a controlled phase shift and hence effectively rotate the polarization profile. By translating the mirror along the beam propagation direction, we varied $\theta(t)$ with a speed of $\sim 2\pi$ rad/s. This is analogous to rotating the polarization direction of a beam to induce high-clarity Haidinger's brush (36).

The participants covered their nonviewing eye with an eye patch. The headrest included a chin rest with a variable height and a forehead rest bar. The location of the user lens was optimized for each participant.

Fig. 2, *i* shows the camera-imaged intensity profiles that were observed. The $|\Psi_-\rangle$ state inducing nine fringes was termed "many," while the $|\Psi_+\rangle$ state inducing five fringes was termed "fewer." In the study, the participants only observed beams shown in Fig. 2, *i*, and the red circles bound the area ($\sim 2^\circ$ in field of vision) with good intensity and high-quality phase structure that the participants were instructed to observe.

Participants. Experimental participants were recruited from the Institute for Quantum Computing and the School of Optometry and Vision Science at the University of Waterloo. The complete study involved two experimental sessions. Participation required written informed consent, and all participants received CAD$15 per session in appreciation for their time. All research procedures received approval from the University of Waterloo Office of Research Ethics, and all participants were treated in accordance with the Declaration of Helsinki.

A total of 12 participants were recruited. Of these, two participants did not complete the study. One participant voluntarily withdrew after reporting that they saw many floating features which obscured the stimulus during the familiarization period. The second participant reported discomfort, and so they were immediately removed from the study. Therefore, 10 participants completed the experiment.

Psychophysical Procedure. Participants were tested on a psychophysical discrimination task over two experimental sessions. A familiarization period occurred during session 1 whereby the participants viewed the "many" beam while the mirror in the setup was translated, inducing a rotation of the pattern either clockwise or counterclockwise. Participants were asked to observe the region bounded by the red circles in Fig. 2, *i* and indicate the direction of rotation. Participants began the main experiment after five consecutive correct answers in the familiarization task.

After familiarization, participants performed the main psychophysical task. A 5-min dark adaptation period occurred at the start of each session. All participants observed the beam with their preferred eye, and the other eye was patched. Each session was composed of five blocks with 10 trials each. The trials were separated by $\sim$5 s, and no break occurred between blocks. At the start of a block, participants observed two alternating presentations of the "many" and "fewer" beams, each lasting up to 10 s. The correct label for each beam was told to the participants. After completing the alternating presentations, participants performed the discrimination task. For each trial, a Python 3.6 random number generator was used to determine which state the participant would view. Each trial was presented for no more than 15 s (excluding the instances where the participant wished to adjust their position), and the participant verbally indicated the perceived trial type. C.K. was in charge of initializing the QWP orientation via the motorized stage, and he provided the real-time corrective feedback to the participant after each trial. D.S., who did not know the orientation of the QWP in the trials, was present to answer any questions that the participant might have during the study. In total, each participant completed 100 trials across two testing sessions (5 blocks $\times$ 10 trials per block $\times$ 2 sessions).

Data Availability. All of the information and protocols needed to replicate the experiment are fully described in the manuscript. All datasets generated during the current study are available from the corresponding author on request.

ACKNOWLEDGMENTS. This work was supported by the Canadian Excellence Research Chairs program, the Velux Stiftung Foundation (Grant 1188), the Natural Sciences and Engineering Research Council of Canada Grants RGPIN-2018-04989, RPIN-05394, and RGPAS-477166, the Collaborative Research and Training Experience program, and the Canada First Research Excellence Fund. We are thankful to Alex Mitrovic for his help with machining. We are also very thankful to the editor and the referees for providing useful suggestions and comments that resulted in article improvements. D.A.P. is thankful to Dusan Mirkovic for useful discussions.

1. S. M. Barnett, M. Babiker, M. J. Padgett, Optical orbital angular momentum. *Philos. Trans. A Math. Phys. Eng. Sci.* **375**, 20150444 (2017).
2. G. Molina-Terriza, J. P. Torres, L. Torner, Twisted photons. *Nat. Phys.* **3**, 305–310 (2007).
3. V. Garces-Chavez, D. McGloin, H. Melville, W. Sibbett, K. Dholakia, Simultaneous micromanipulation in multiple planes using a self-reconstructing light beam. *Nature* **419**, 145–147 (2002).
4. G. Siviloglou, J. Broky, A. Dogariu, D. Christodoulides, Observation of accelerating airy beams. *Phys. Rev. Lett.* **99**, 213901 (2007).
5. S. Schwarz *et al.*, Talbot effect of orbital angular momentum lattices with single photons. *Phys. Rev.* **101**, 043815 (2020).
6. L. Allen, M. W. Beijersbergen, R. J. C. Spreeuw, J. P. Woerdman, Orbital angular momentum of light and the transformation of Laguerre-Gaussian laser modes. *Phys. Rev. A* **45**, 8185–8189 (1992).
7. V. I. Bazhenov, M. V. Vasnetsov, M. S. Soskin, Laser beams with wave front screw dislocations. *Pisma Zh. Eksp. Teor. Fiz.* **52**, 1037–1039 (1990).
8. A. Mair, A. Vaziri, G. Weihs, A. Zeilinger, Entanglement of the orbital angular momentum states of photons. *Nature* **412**, 313–316 (2001).
9. M. F. Andersen *et al.*, Quantized rotation of atoms from photons with orbital angular momentum. *Phys. Rev. Lett.* **97**, 170406 (2006).
10. N. Simpson, K. Dholakia, L. Allen, M. Padgett, Mechanical equivalence of spin and orbital angular momentum of light: An optical spanner. *Optics Lett.* **22**, 52–54 (1997).
11. M. Ritsch-Marte, Orbital angular momentum light in microscopy. *Phil. Trans. Math. Phys. Eng. Sci.* **375**, 20150437 (2017).
12. J. Wang *et al.*, Terabit free-space data transmission employing orbital angular momentum multiplexing. *Nat. Photon.* **6**, 488–496 (2012).
13. M. Padgett, R. Bowman, Tweezers with a twist. *Nat. Photon.* **5**, 343–348 (2011).
14. C. Maurer, A. Jesacher, S. Fürhapter, S. Bernet, M. Ritsch-Marte, Tailoring of arbitrary optical vector beams. *New J. Phys.* **9**, 78 (2007).
15. L. Marrucci, C. Manzo, D. Paparo, Optical spin-to-orbital angular momentum conversion in inhomogeneous anisotropic media. *Phys. Rev. Lett.* **96**, 163905 (2006).
16. D. Sarenac *et al.*, Generation of a lattice of spin-orbit beams via coherent averaging. *Phys. Rev. Lett.* **121**, 183602 (2018).
17. H. Rubinsztein-Dunlop *et al.*, Roadmap on structured light. *J. Optic.* **19**, 013001 (2016).
18. G. Milione *et al.*, 4$\times$ 20 gbit/s mode division multiplexing over free space using vector modes and a q-plate mode (de) multiplexer. *Optics Lett.* **40**, 1980–1983 (2015).
19. L. Marrucci *et al.*, Spin-to-orbital conversion of the angular momentum of light and its classical and quantum applications. *J. Optic.* **13**, 064001 (2011).
20. Q. Zhan, Cylindrical vector beams: From mathematical concepts to applications. *Adv. Optic Photon* **1**, 1–57 (2009).
21. F. Cardano *et al.*, Polarization pattern of vector vortex beams generated by q-plates with different topological charges. *Appl. Optic.* **51**, C1–C6 (2012).

22. E. J. Galvez, S. Khadka, W. H. Schubert, S. Nomoto, Poincaré-beam patterns produced by nonseparable superpositions of Laguerre–Gauss and polarization modes of light. *Appl. Optic.* **51**, 2925–2934 (2012).
23. C. Rosales-Guzmán, B. Ndagano, A. Forbes, A review of complex vector light fields and their applications. *J. Optic.* **20**, 123001 (2018).
24. T. Konrad, A. Forbes, Quantum mechanics and classical light. *Contemp. Phys.* **60**, 1–22 (2019).
25. M. McLaren, T. Konrad, A. Forbes, Measuring the nonseparability of vector vortex beams. *Phys. Rev. A* **92**, 023833 (2015).
26. W. Haidinger, Ueber das directe erkennen des polarisirten lichts und der lage der polarisationsebene. *Annalen der Physik* **139**, 29–39 (1844).
27. G. P. Misson, B. H. Timmerman, P. J. Bryanston-Cross, Human perception of visual stimuli modulated by direction of linear polarization. *Vis. Res.* **115**, 48–57 (2015).
28. G. P. Misson, S. J. Anderson, The spectral, spatial and contrast sensitivity of human polarization pattern perception. *Sci. Rep.* **7**, 16571 (2017).
29. G. P. Misson, S. E. Temple, S. J. Anderson, Computational simulation of human perception of spatially dependent patterns modulated by degree and angle of linear polarization. *J. Opt. Soc. Am. A Opt. Image Sci. Vis.* **36**, B65–B70 (2019).
30. G. Horváth, G. Horváth, D. Varju, *Polarized Light in Animal Vision: Polarization Patterns in Nature* (Springer Science & Business Media, 2004).
31. H. W. Forster, The clinical use of the Haidinger's brushes phenomenon. *Am. J. Ophthalmol.* **38**, 661–665 (1954).
32. E. Naylor, A. Stanworth, The measurement and clinical significance of the haidinger effect. *Trans. Ophthalmol. Soc. U.K.* **75**, 67 (1955).
33. P. L. Müller *et al.*, Perception of Haidinger brushes in macular disease depends on macular pigment density and visual acuity. *Invest. Ophthalmol. Vis. Sci.* **57**, 1448–1456 (2016).
34. D. A. VanNasdale, A. E. Elsner, A. Weber, M. Miura, B. P. Haggerty, Determination of foveal location using scanning laser polarimetry. *J. Vis.* **9**, 21–21 (2009).
35. W. A. Shurcliff, Haidinger's brushes and circularly polarized light. *J. Opt. Soc. Am.* **45**, 399–399 (1955).
36. S. Coren, The use of Haidinger's brushes in the study of stabilized retinal images. *Behav. Res. Methods Instrum.* **3**, 295–297 (1971).
37. G. Horváth *et al.*, Celestial polarization patterns sufficient for Viking navigation with the naked eye: Detectability of Haidinger's brushes on the sky versus meteorological conditions. *Roy. Soc. Open Sci.* **4**, 160688 (2017).
38. M. Berry, Optical vortices evolving from helicoidal integer and fractional phase steps. *J. Optic. Pure Appl. Optic.* **6**, 259–268 (2004).
39. G. P. Misson, A Mueller matrix model of Haidinger's brushes. *Ophthalmic Physiol. Optic.* **23**, 441–447 (2003).
40. M. Rothmayer *et al.*, Nonlinearity in the rotational dynamics of haidinger's brushes. *Appl. Optic.* **46**, 7244–7251 (2007).
41. G. P. Misson, S. E. Temple, S. J. Anderson, Computational simulation of haidinger's brushes. *J. Opt. Soc. Am.* **35**, 946–952 (2018).
42. J. Maxwell, "Manuscript on experiments on the cause of Haidinger's brushes" in *The Scientific Letters and Papers of James Clerk Maxwell* (Taylor and Francis, 1850) pp. 199–204.
43. H. von Helmholtz, *Treatise on Physiological Optics Treatise on Physiological Optics (1867)* (Optical Society of America, Rochester, NY, 1925).
44. L. J. Bour, Polarized light and the eye. *Vis. Optic. Instrum.* **1**, 310–325 (1991).
45. R. W. Knighton, X. R. Huang, Linear birefringence of the central human cornea. *Investig. Ophthalmol. Vis. Sci.* **43**, 82–86 (2002).
46. International Commission on Non-Ionizing Radiation Protection, Revision of guidelines on limits of exposure to laser radiation of wavelengths between 400 nm and 1.4 μm. *Health Phys.* **79**, 431–440 (2000).
47. M. Beijersbergen, R. Coerwinkel, M. Kristensen, J. Woerdman, Helical-wavefront laser beams produced with a spiral phaseplate. *Optic Commun.* **112**, 321–327 (1994).
48. T. D. Wickens, *Elementary Signal Detection Theory* (Oxford University Press, 2002).
49. P. S. Bernstein *et al.*, Lutein, zeaxanthin, and meso-zeaxanthin: The basic and clinical science underlying carotenoid-based nutritional interventions against ocular disease. *Prog. Retin. Eye Res.* **50**, 34–66 (2016).
50. B. Hochheimer, H. A. Kues, Retinal polarization effects. *Appl. Optic.* **21**, 3811–3818 (1982).
51. J. N. Tinsley *et al.* Direct detection of a single photon by humans. *Nat. Commun.* **7**, 12172 (2016).
52. M. Loulakis, G. Blatsios, C. Vrettou, I. Kominis, Quantum biometrics with retinal photon counting. *Phys. Rev. Appl.* **8**, 044012 (2017).
53. N. Sim, M. F. Cheng, D. Bessarab, C. M. Jones, L. A. Krivitsky, Measurement of photon statistics with live photoreceptor cells. *Phys. Rev. Lett.* **109**, 113601 (2012).
54. A. Dodel *et al.*, Proposal for witnessing non-classical light with the human eye. *Quantum* **1**, 7 (2017).